Originally published as:

Constructive optimization of electrode locations for target-focused resistivity monitoring

Florian M. Wagner[12], Thomas Günther[3], Cornelia Schmidt-Hattenberger[1], and Hansruedi Maurer[2]

ABSTRACT

Crosshole resistivity tomography has received consideration as a tool for quantitative imaging of carbon dioxide stored in deep saline aquifers. With regard to the monitoring responsibility of site operators and the substantial expenses associated with permanent downhole installations, optimized experimental design gains particular importance. Based on an iterative appraisal of the formal model resolution matrix, we present a method to estimate optimum electrode locations along the borehole trajectories with the objective to maximize the imaging capability within a prescribed target horizon. For the presented crosshole case, these layouts are found to be symmetric, exhibiting refined electrode spacings within the target horizon. Our results demonstrate that a sparse, but well conceived set of electrodes can provide a large part of the information content offered by comparably dense electrode distributions. In addition, the optimized layout outperforms equidistant setups with the same number of electrodes since its resolution is focused on the monitoring target. The optimized electrode layouts presented provide a powerful and cost-efficient opportunity to complement permanent installations, particularly at, but not limited to, future CO_2 storage sites. Although preliminarily developed to support the design of crosshole resistivity layouts, our approach is directly applicable to other survey geometries including surface and surface-to-hole acquisitions.

[0] [1]Helmholtz Centre Potsdam, GFZ German Research Centre for Geosciences, Potsdam, Germany. E-Mail: florian.wagner@gfz-potsdam.de; cornelia.schmidt-hattenberger@gfz-potsdam.de
[2]ETH Zurich, Institute of Geophysics, Zurich, Switzerland. E-Mail: hansruedi.maurer@erdw.ethz.ch
[3]Leibniz Institute for Applied Geophysics, Hannover, Germany. E-Mail: thomas.guenther@liag-hannover.de

INTRODUCTION

Characterization of subsurface fluid transport by means of time-lapse electrical resistivity is a well established method in near-surface geophysics (e.g. Daily et al., 1992; Slater et al., 2000; Binley and Kemna, 2005; Perri et al., 2012). In particular the application of permanent electrode installations offers opportunities to study the spatio-temporal evolution of dynamic subsurface processes and allows for the derivation of underlying aquifer properties such as fluid saturation, solute concentration, and temperature over large temporal scales (e.g. Wilkinson et al., 2010; Deceuster et al., 2013). Recently, it has been recognized that the method, on the strength of its high sensitivity to compositional pore fluid changes, is well suited to monitor the migration of carbon dioxide stored in deep saline aquifers (Ramirez et al., 2003; Christensen et al., 2006; Bergmann et al., 2012; Breen et al., 2012; Carrigan et al., 2013). Although many methodological and practical aspects are essentially similar, the transferability to deep reservoir surveillance is not straightforward and entails specific methodological challenges in addition to the obvious complexity of installing permanent electrode systems at typical reservoir depths of a few kilometers. Moreover, the monitoring responsibility of site operators as well as the associated installation costs require particularly well conceived experimental designs.

Substantial advances have been made in geophysical survey design within the last decades (see Maurer et al., 2010, for a review). In electrical resistivity imaging, most experimental design studies have concentrated on the identification of individual four-point configurations that optimally exploit the information content offered by modern multi-electrode arrays (e.g. Stummer et al., 2004; Wilkinson et al., 2006; Furman et al., 2007; Coscia et al., 2008; Loke et al., 2014).

The geological storage of carbon dioxide is a long-term process and downhole monitoring systems are expected to provide information over several decades, desirably even

within the post-closure phase of a given site. This means that the timescale of investigation allows for the employment of both standard and individually tailored electrode configurations. The information contents of traditional and optimized configurations may differ, but in any case, they are ultimately limited by the underlying electrode layout. In consequence, the initial installation design concerning the individual sensor positions gains particular importance, since these positions can be chosen only once, while the individual configurations in the measurement schedule can be readily controlled and adapted remotely.

After a brief discussion of the relevant theory, we present a method to constructively optimize electrode locations by means of an iterative appraisal of the formal model resolution matrix. Subsequently, the method is applied to the Ketzin pilot site, Germany, where electrical resistivity tomography (ERT) is part of a multi-disciplinary monitoring program to monitor the migration of injected CO_2 (Martens et al., 2012; Köhler et al., 2013). The crosshole electrode layout resulting from the optimization process is compared to the current equidistant installation at the site with regard to the monitoring performance for a realistic CO_2 plume migration scenario. Based on this synthetic modeling study and our practical experience after more than five years of operation, the Ketzin electrode setup is evaluated and benefits and limitations of an optimized alternative are discussed. Provided that a priori information on the subsurface target is available, our findings can assist practitioners to optimally design high-resolution and cost-efficient resistivity monitoring systems especially for, but not limited to, future CO_2 storage sites.

THEORY

Forward modeling and tomographic inversion

In tomographic experiments one aims to derive an estimate of the model parameter distribution $\mathbf{m_{est}}$ from a set of observed data points $\mathbf{d_{obs}}$, commonly measured on the model boundary or within its interior (e.g. in the case of electrode-equipped boreholes). Similar to most geophysical problems, the geoelectrical problem is solved iteratively, as the relationship between subsurface resistivities and measured apparent resistivities is described by the nonlinear forward operator $\mathbf{f}$. After linearization around a model $\mathbf{m_k}$ the problem can be written as

$$\Delta \mathbf{d} = \mathbf{d_{obs}} - \mathbf{f}(\mathbf{m_k}) = \mathbf{G}(\mathbf{m_{true}} - \mathbf{m_k}). \quad (1)$$

Note that $\mathbf{d_{obs}}$ and $\mathbf{f}(\mathbf{m_k})$ are subject to measurement and modeling errors, respectively. The Jacobian matrix $\mathbf{G}$ comprises the sensitivities of the logarithmized measurements with respect to logarithmic parameter perturbations

$$\mathbf{G}_{i,j} = \frac{\partial \log(\rho_i^a)}{\partial \log(\rho_j)} = \frac{\rho_j}{\rho_i^a} \frac{\partial \rho_i^a}{\partial \rho_j}, \quad (2)$$

where ρ_i^a is the simulated apparent resistivity for the ith electrode array and ρ_j is the resistivity of the jth model cell. The forward calculation used in this study follows the approach by Rücker et al. (2006), where the sensitivities are derived by summation over the potential gradients obtained from a finite element simulation on unstructured meshes (Günther et al., 2006).

The corresponding linearized inverse problem can be written as

$$\mathbf{m_{est}} = \mathbf{m_k} + \mathbf{G}^{-g}\Delta \mathbf{d}, \quad (3)$$

where the generalized Gauss-Newton type inverse operator $\mathbf{G}^{-g}$ reads (e.g. Aster et al., 2012)

$$\mathbf{G}^{-g} = (\mathbf{G}^T\mathbf{D}^T\mathbf{D}\mathbf{G} + \lambda\mathbf{C}^T\mathbf{C})^{-1}\mathbf{G}^T\mathbf{D}^T\mathbf{D}. \quad (4)$$

Here, $\mathbf{D}$ is a data weighting matrix containing the reciprocals of the individual data errors on the main diagonal, while λ controls the amount of regularization induced by the discretized first-order derivative operator $\mathbf{C}$. For a detailed description of the inversion scheme used in this study, the reader is referred to Günther et al. (2006) and references therein.

Image appraisal and experimental design

The geoelectrical inverse problem is inherently non-unique. When interpreting tomographic images, it is therefore generally advisable to take measures of uncertainty into account. Several image appraisal quantities exist that can assist practitioners in an ascertainment of regions, which resemble the true subsurface more likely than others. In addition, these quantities allow to optimize experimental designs prior to deployment, i.e. finding setups by means of synthetic analyses, that would maximize these quantities when realized in the field. The cumulative sensitivity of a model region, obtained by summation over the absolute values in each column of the Jacobian matrix $\mathbf{G}$ (equation 2), is often used as a first means of image appraisal. Yet Kemna (2000) underlines that high sensitivity does not guarantee high resolution and should rather be interpreted as a favoring factor. A more rigorous measure is the formal model resolution matrix, which is obtained by combining the linear approximations in equations 1 and 3:

$$\begin{aligned} \mathbf{m_{est}} &\approx \mathbf{G}^{-g}\mathbf{G}\mathbf{m_{true}} \\ &\approx \mathbf{R_m}\mathbf{m_{true}}. \end{aligned} \quad (5)$$

The model resolution $\mathbf{R_m} = \mathbf{G}^{-g}\mathbf{G}$ is a M by M matrix, where M represents the number of model parameters. It combines the forward and inverse operators and relates the unknown true model parameters to their respective estimates. Although strictly valid only for truly linear problems, the model resolution can provide detailed diagnostics on the imaging characteristics, as it combines both sensitivity and linear independence of the individual measurements involved in addition to the regularization term

(e.g. Friedel, 2003). Despite the drawback of being computationally expensive, the model resolution is the preferred choice in ERT experimental design studies and has proven to be a good forecaster of the eventual inversion performance (Stummer et al., 2004; Coscia et al., 2008; Wilkinson et al., 2006, 2010, 2012; Loke et al., 2014). Individual columns of $\mathbf{R_m}$, so called *point spread functions* (PSF), show how a resistivity perturbation in the subsurface is mapped into the final inversion image (Oldenborger and Routh, 2009). A common approach to condense this large amount of information to the entire model region is to use the main diagonal values as a degree of resolution for a specific model parameter.

When using unstructured discretizations, the sensitivity of a model parameter (and thereby its resolution) is dependent on the corresponding cell size, since resistivity perturbations in larger cells have a more significant influence on a single measurement compared to smaller cells. While one could directly normalize the main diagonal entries by the cell sizes, Friedel (2003) introduced a more practical quantity, the *radius of resolution*, which is defined as

$$r_i = \sqrt{\frac{A_i}{\pi \cdot \mathrm{diag}(\mathbf{R_m})_i}} \quad (6)$$

for two-dimensional discretizations, where A_i is the area of the ith model cell. If the parameter of a model cell was perfectly resolved ($\mathrm{diag}(\mathbf{R_m})_i$=1), r_i would equal the radius of a circle with the same area as the model cell, translating the diagonal entries of the model resolution matrix into a readily understandable measure that accounts for unstructured discretizations. Figure 1 shows the PSF of a cell in the central region between two boreholes and the corresponding radius of resolution 6.1 m calculated for a complete noise-free pole-pole data set with a homogeneous background. PSF values are normalized by the maximum value.

Figure 1 shows that the PSF and the radius of resolution independently mark out a circular area of approximately the same size around the cell of investigation and thereby emphasizes the validity of the common approach to only use the diagonal entries as a quantitative measure of resolution. This is in agreement with the recent finding of Loke et al. (2014), who demonstrated that optimizations of individual four-point configurations based on PSF measures do not notably improve the information content of the resulting arrays compared to optimizations based exclusively on the diagonal entries, while the former is computationally considerably more cumbersome. Yet it should be emphasized that the comparable performances of the diagonal entries and PSF measures during array optimizations are by no means evidence of their equality. High resolution values correspond to high PSF, but low diagonal values of the resolution matrix may not account for potentially severe off-diagonal entries.

In this paper, we adopt the definition of the resolution radius to account for the unstructured discretizations
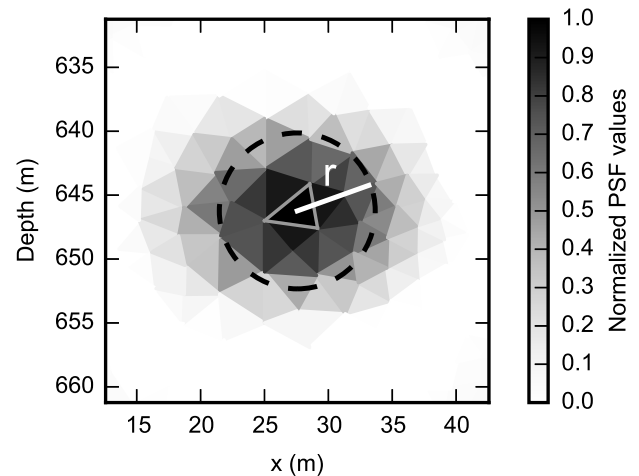

Figure 1: Normalized point spread function plot calculated for a crosshole experiment measured with a noise-free pole-pole data set in a homogeneous medium. The triangular cell under investigation is framed and located in the central region between two boreholes at $x = 0$ m and $x = 50$ m (not shown). The dashed circle is drawn around the center of the cell with the corresponding *radius of resolution* (after Friedel, 2003) of 6.1 m.

used, to compare resolutions of different setups, and, most importantly, to define detection limits for different electrode layouts with regard to resolvable CO_2 plume thicknesses.

OPTIMIZATION METHOD

The optimization strategy used in this study is outlined in Figure 2:

1. We start with the determination of an initial model $\mathbf{m}_0$ that resembles our a priori information on the subsurface resistivity distribution. This information could be obtained from previous geophysical surveys and wireline induction logs. Particular attention is to be paid to the target within the model, as it defines the region where the optimized layout is sought to have its highest resolution.

2. Candidate positions for possible electrode deployment are assigned along the borehole trajectories, ideally under consideration of practical constraints such as the prescription of a smallest feasible electrode spacing or the definition of depth intervals where electrode deployment may be permitted due to technical reasons. The number of candidate electrodes should be chosen large enough (under consideration of computational resources), so that the optimized layouts are not biased by the preselected candidates.

3. Based on the geometrical specifications from the previous steps, the model domain is spatially discretized.
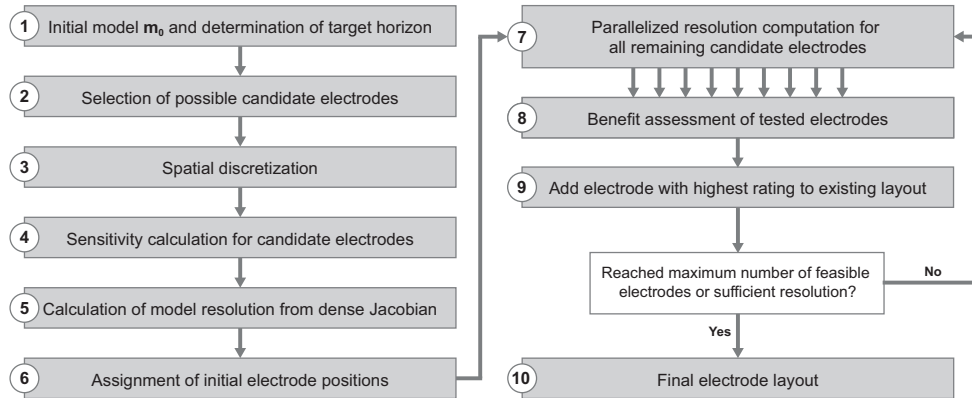
Figure 2: Schematic outline of the proposed optimization procedure.

4. Subsequently, the Jacobian matrix for $\mathbf{m}_0$ is calculated based on a complete data set (e.g. pole-pole) involving all candidate electrodes.

5. The maximum resolution possible with the chosen candidate electrodes is computed as a reference based on the dense Jacobian matrix obtained in the previous step. This calculation is likely to be expensive, since the Jacobian matrix scales with the model parameters and measurements involved. Calculating the approximate Hessian matrix ($\mathbf{G}^T\mathbf{G}$ in equation 4) has also been identified as the bottleneck in resolution studies related to global body wave tomography (Boschi, 2003; Soldati et al., 2006). To cope with the associated computational effort, we have parallelized the computation of $\mathbf{G}^T\mathbf{G}$ and further exploited its inherent symmetry by only calculating and storing the lower (or upper) triangular entries including the main diagonal (Wang et al., 2013).

6. To start the optimization process, a subset of the candidate electrodes is assigned to the initial electrode layout.

7. The model resolution is computed independently for each of the remaining candidate electrodes in parallel. Hereby, the individual rows of the Jacobian matrix are assembled with sensitivities of the complete data set (calculated in step 4) that correspond to measurements involving the currently evaluated electrode and all other electrodes already present in the survey layout.

8. During each iteration of the optimization process, the benefit of electrode k is evaluated in terms of a resolution improvement ζ_k normalized by the maximum possible resolution according to

$$\zeta_k = \text{median}\left(\frac{R_m^{j,j}(k)}{R_m^{j,j}(\text{dense})}\right). \qquad (7)$$

Here, j iterates over all cells located within the target. Hence, only resolution improvements in the target horizon are accounted for in this study. Normalization in equation 7 is necessary to counterbalance the general high resolution close to the electrodes (Stummer et al., 2004). For the same reason we chose the more robust median operator, since the mean can easily be deteriorated by a few very high values close to the electrodes.

9. After each iteration, the electrode with the highest benefit ζ_k is added to the survey layout.

10. Iterative repetition of steps 7-9 can be terminated when the number of maximum feasible or desired electrodes is reached or the resolution does not notably improve further.

APPLICATION AND DISCUSSION

Optimized design for a homogeneous model

To demonstrate the method, a homogeneous crosshole scenario with a borehole spacing of 50 m and a target horizon of 30 m thickness is considered as outlined in Figure 3.

Within the target horizon, possible candidate electrodes are arranged with a vertical spacing of 1 m. Above and below the target horizon candidate electrodes are arranged with a spacing of 2.5 m. The maximum edge length of the parameter discretization is equal to the electrode spacing close to the boreholes and ≈ 7 m between the boreholes. To calculate the forward responses, the mesh was further refined by bisecting each edge. For the sensitivity calculation, we use a complete, noise-free pole-pole data set with $n(n-1)/2$ non-reciprocal measurements, where n denotes the number of electrodes. Short-distance pole-pole measurements with unit electrode spacings of 1-3 are omitted to avoid near-electrode artifacts while keeping the number of cells reasonably small. The reference resolution (step 5 in Figure 2) is calculated based on 9,591 measurements with 142 candidate electrodes. The absolute values of the model resolution are influenced by the regularization strength λ (equation 4). However, the optimization
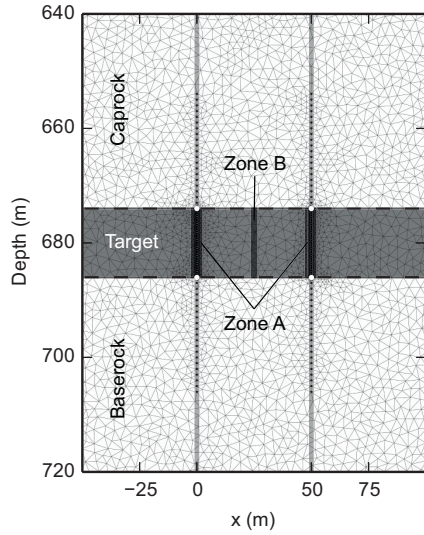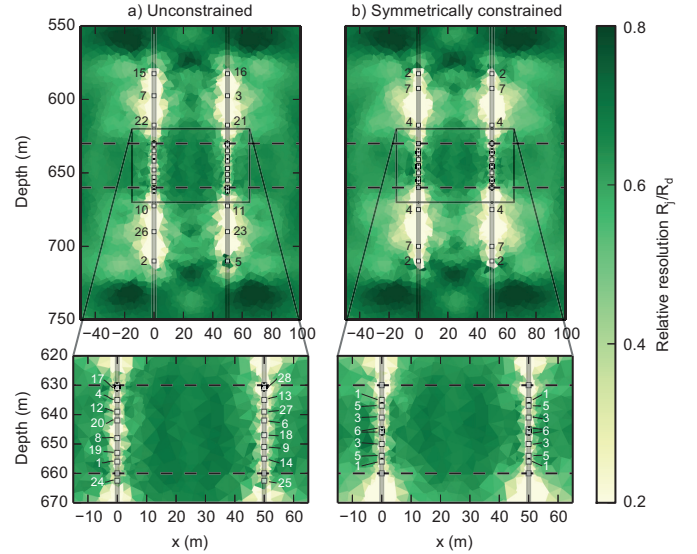
Figure 3: Three-layer crosshole scenario under investigation. White and black dots indicate initial and candidate electrode positions, respectively.


Figure 4: Optimized setups for a homogeneous background model. (a) One candidate electrode is added per iteration. (b) The best-rated electrode and its 3 symmetric counterparts are added during each iteration. The relative resolution is color-coded. Zoomed sections of the reservoir horizon (bounded by the dashed lines) are provided in the lower part of the figure.

itself is not sensitive to the amount and type of regularization when relative resolution improvements are evaluated as in equation 7 (Loke et al., 2010). Following Coscia et al. (2008), we use $\lambda = 10 \operatorname{diag}(\mathbf{G}^T\mathbf{G})$. To start the optimization process, an initial survey layout of four electrodes has been selected with two electrodes placed at the top and bottom boundaries of the target horizon in each well (represented by white dots in Figure 3).

Figure 4a shows the optimized electrode positions after 28 iterations and the relative resolution obtained with a total of 32 electrodes including the initial four. The relative resolution denotes the ratio of the resolution values from the subset layout (R_j) and the dense layout (R_d). Hence, relative resolution values close to 1 correspond to regions where the subset layout achieves a resolution comparable to the dense layout. The numbers in Figure 4 mark the order of selection and thereby indicate the priority of each individual electrode position.

The resulting optimized setup is symmetric with respect to the x and y axes. As expected based on equation 7, the electrode spacing is refined within the target horizon, while a few more widely spaced electrodes are selected in the caprock and baserock regions. Note that this was also the case when more candidate electrodes were assigned outside of the target. The relative resolution within the target horizon ranges up to 85.7% with a mean value of 50.1%. Figure 4b shows a similar result of the optimization process when this two-fold symmetry was presumed, i.e. the highest rated electrode and its three symmetric counterparts were added during each iteration, which effectively reduced the computational effort by a factor of 4. For the symmetric crosshole scenarios considered in this study in the absence of dipping horizons or complex geologic features, the algorithm yields symmetric electrode layouts aside from small scale deviations as evident in the

zoomed section of Figure 4a. To reduce the computational demand, the symmetry constraint is therefore used throughout all subsequent optimizations.

Figure 5 shows the resolution improvement and illustrates the selection behavior throughout the entire optimization process, i.e., until no more candidate electrodes are available. The curves show the mean relative model resolution within different regions over the course of iterations and thereby as a function of the number of electrodes. Dots denote the selection of electrode positions within the target horizon, whereas crosses denote non-target electrodes.

The red curve shows the mean relative resolution within the target averaged over all model cells in a distance of 2 m away from the electrodes (corresponding to zone A in Figure 3). During an alternating selection of electrodes inside and outside of the target, the model resolution close to the boreholes increases almost linearly until no more candidate electrode positions within the target horizon are available. This is evidenced in Figure 5 by the notable flattening of the resolution improvement after the inclusion of 96 electrodes, followed exclusively by the selection of non-target electrodes. For the entire target horizon (blue curve), and especially for the central region between both boreholes (green curve; corresponding to zone B in Figure 3), the relative resolution curves exhibit larger ordinate intercepts, generally higher values, and the gain in resolution drops earlier.

Figures 4 and 5 reveal that a large proportion of the information content offered by the dense layout (with 142 electrodes) can be achieved with only a few well-chosen electrodes. This particularly applies for the region in be-
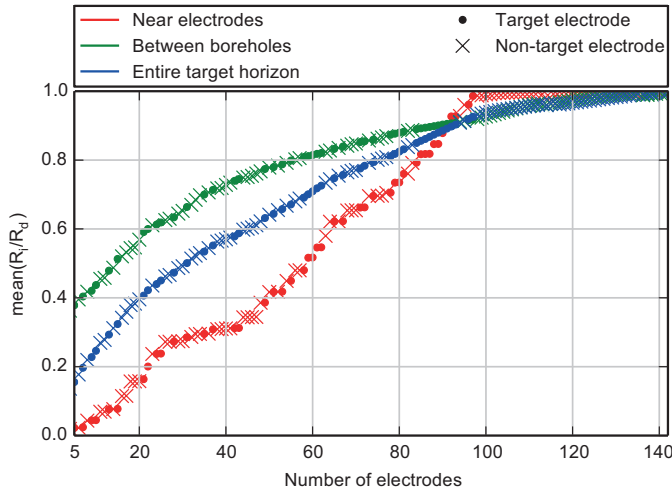
Figure 5: Evolution of the mean relative model resolution within the target horizon during the optimization process. Relative resolution values are averaged near the electrodes (red curve; corresponding to zone A in Figure 3), in the central region between the boreholes (green curve; corresponding to zone B in Figure 3), and for the entire target horizon (blue curve). Dots and crosses denote the selection of target and non-target electrodes, respectively.

tween both boreholes, whereas the small-scale resolution near the boreholes can always be improved by deploying additional electrodes.

The determination of an optimum number of electrodes is not obvious and depends on the number of possible candidate positions allowed. In this example, 65 to 82 percent of the model resolution between the boreholes can be achieved with a practical number of 15 to 30 electrodes per well. In summary, the optimized layout is symmetric and has smaller electrode spacings in the target region. Yet a few more sparsely distributed caprock and baserock electrodes are equally important for the overall model resolution, since these electrodes offer new linear independent configurations to be measured.

Impact of subsurface heterogeneity

As a first means to evaluate the impact of subsurface heterogeneities, we consider deviations of the resistivity of the target horizon (ρ_t) from the background resistivity (ρ_0). Figure 6 illustrates the sensitivity of a single pole-pole measurement, if the target horizon is four times as conductive than the surrounding layers (a) and vice versa (b).

If the target resistivity is lower (Figure 6a), the sensitivity within the target increases due to the higher current density. If the target layer is more resistive (Figure 6b), the positive sensitivity is diverted into the more conductive adjacent strata. Between the electrodes, where the sensitivity is usually the strongest, absolute values of the negative sensitivity do not drop significantly. Note that this effect is amplified by the scaling of the Jacobian ma-
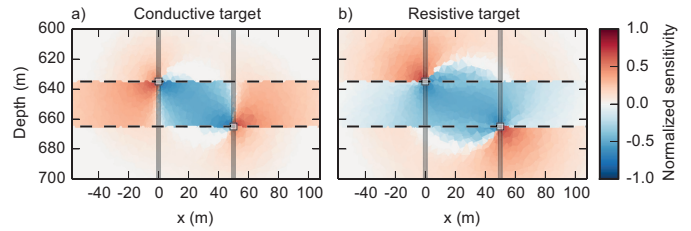
Figure 6: Normalized sensitivity of a single pole-pole measurement for a conductive (a) and a resistive target horizon (b). The resistivity ratio of the target compared to the surrounding layers (ρ_t/ρ_0) is 0.25 and 4, respectively.

trix in equation 2 to account for logarithmic data and parameters.
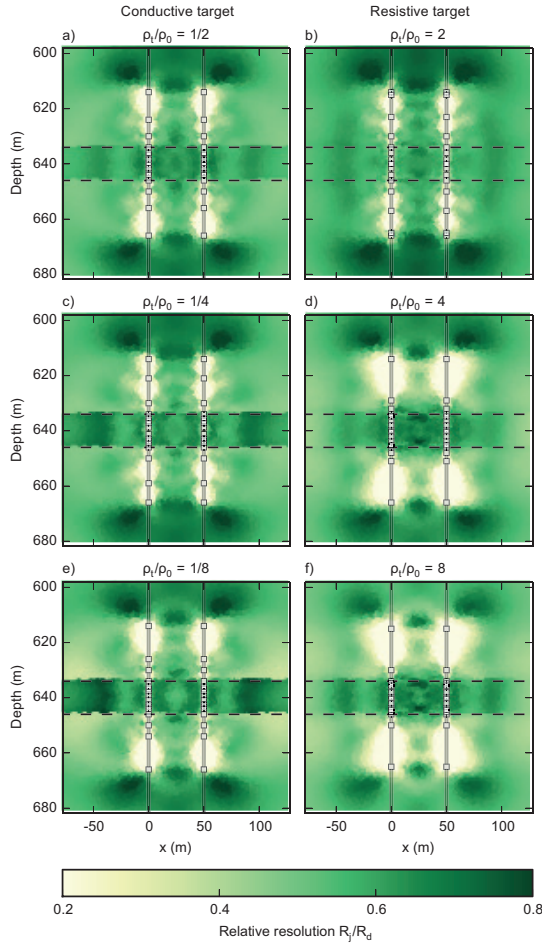
Figure 7 shows the result of the optimization process for a conductive and a resistive target with different contrasts ρ_t/ρ_0. Each optimization was terminated after 7 iterations, which corresponds to a total of 32 electrodes including the initial four.

Figure 7 reveals no significant change of the optimized layouts, when the resistivity of the target is altered by a factor of two (Figure 7a, b). For a resistivity ratio of 0.25 (Figure 7c), the relative resolution within the target increases due to the increased sensitivity values observed in Figure 6a. The optimized electrode positions, however, do not change notably. Increasing the conductivity of the target even further ($\rho_t/\rho_0 = 0.125$) causes a slight shift of the caprock and baserock electrodes towards the more conductive reservoir. For the resistive case, increasing ρ_t/ρ_0 to values of four (Figure 7d) and eight (Figure 7f) leads to a significant confinement of electrodes within the target. As discussed earlier, higher current density in the more conductive caprock and baserock layers divert part of the sensitivity away from the target horizon (Figure 6b). Hence, electrodes outside of the target can contribute less to the resolution within the zone of interest and are therefore penalized during the optimization process.
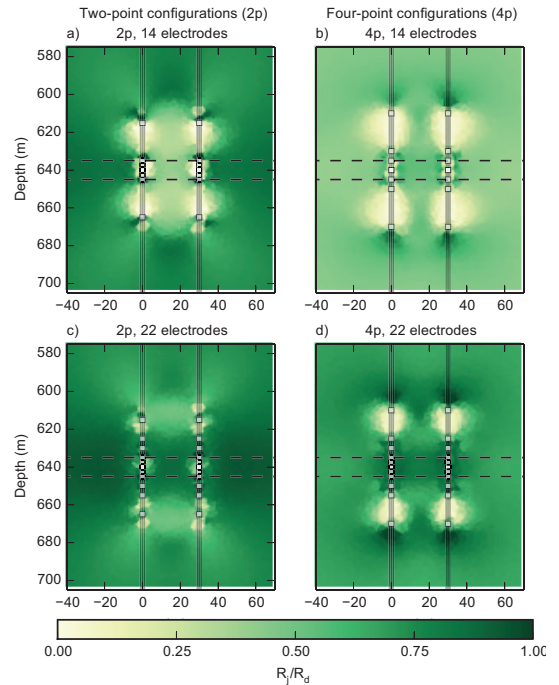
Effect of four-point configurations

Optimizations up to this point were based on a complete set of pole-pole measurements with the assumption that the information content offered by a complete data set can be used to adequately characterize the goodness of individual electrode positions. In addition, a complete pole-pole data set has the advantage that all electrodes occur equally often within the measurement schedule. Hence, each candidate electrode is evaluated by reference to the same number of sensitivity kernels. However, it was emphasized by Bing and Greenhalgh (2000) that four-point configurations offer several distinct practical advantages especially under pronounced noise conditions (due to the absence of remote electrodes), which often make them the preferred choice in electrical resistivity imaging.

To assess the influence of the underlying basis configurations, we have performed the optimization on the basis

of a comprehensive four-point data set described by Xu and Noel (1993). That is, the sensitivity kernels of all $n(n-1)(n-2)(n-3)/8$ non-reciprocal four-point configurations, where n is the number of electrodes involved, were used to calculate the model resolutions during the optimization procedure (steps five and seven in Figure 2). In order to keep computational costs within reasonable bounds, the dimensions of the previously discussed examples were scaled down to a borehole spacing of 30 m and a target thickness of 10 m. Furthermore, the spacing of the candidate electrodes was increased to 2.5 m within the target horizon and to 5 m in the caprock and baserock resulting in a total number of 30 candidate electrodes. The comprehensive four-point data set used to compute the reference resolution from the full set of candidate electrodes thus comprises 82,215 sensitivities. In comparison, the complete pole-pole data set consists of $n(n-1)/2 = 435$ measurements. Figure 8 shows the result of both optimization processes obtained after three and five iterations. Note that the four-point based optimization (shown in Figure 8b, d) took nearly 25 times longer than the pole-pole based optimization (shown in Figure 8a, c).

Figure 7: Optimized electrodes (squared markers) and relative resolution (color coded) for a conductive (a, c, e) and a resistive (b, d, f) target horizon with variable resistivity contrasts between target horizon and surrounding layers. The ratio between the target and the background resistivity is given as ρ_t/ρ_0. Each optimization was terminated after 7 iterations corresponding to a total number of 32 electrodes.


Figure 8: Optimized electrodes (squared marker) and relative resolution (color coded) based on a complete pole-pole (a, c) and a comprehensive bipole-bipole data set (b, d). The first and second row show the result after 3 and 5 iterations corresponding to 14 and 22 electrodes, respectively.

Although both optimizations were based on two data sets with different sizes, sensitivity patterns and imaging characteristics, similar layouts result in both cases at early (Figure 8a, b) and later (Figure 8c, d) stages of the optimization process. The conformity of both optimized layouts, i.e. the independence of the underlying configu-

rations, is best understood by revisiting the selection criterion introduced in equation 7 and its implications. An electrode position is chosen, if the measurements with that specific candidate electrode and all other electrodes in the survey layout lead to an improvement of the model resolution within the target region. High resolution values stem from linearly independent measurement configurations with high sensitivities. On the other hand, a mere repetition of individual data points, although advisable in practice for a data quality assessment, does not increase the information content.

To exemplify the information contents offered by a particular data set, one can consider the eigenvalue spectra of the respective Hessian matrix ($\mathbf{G}^T\mathbf{G}$) as the number of non-zero eigenvalues can be related to the number of linear independent measurement configurations (e.g. Maurer et al., 2010; Blome et al., 2011). Figure 9 shows the normalized eigenvalue spectra of the complete pole-pole (solid gray curve) and the comprehensive four-point data set (dashed black curve) from the optimizations shown in Figure 8.
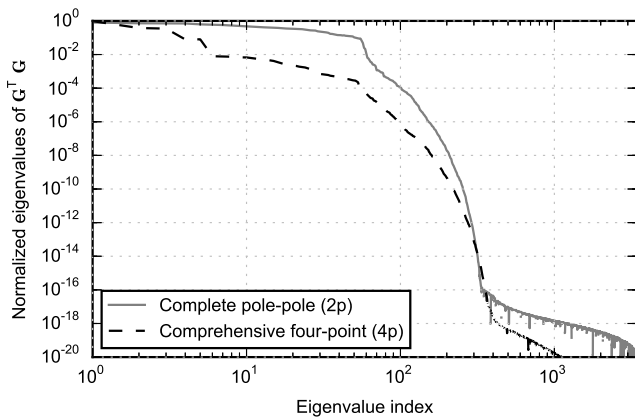
Figure 9: Normalized eigenvalue spectra of the Hessian matrix $\mathbf{G}^T\mathbf{G}$ for a complete pole-pole (solid gray curve) and a comprehensive four-point data set (dashed black curve).

Although the comprehensive four-point data set comprises 189 times more measurements than the complete pole-pole data set, it does not provide more linear independent measurements as evidenced by the concurrent convergence behavior of both eigenvalue spectra down to the limit of numerical precision at 10^{-16}. In other words, the complete pole-pole data set offers the full information content, since all other conceivable measurements can theoretically be derived by superposition.

Therefore, we judge that it is sufficient to use a complete pole-pole data set, which comprises only $n(n-1)/2$ measurements, for the optimization of the electrode locations. The resulting electrode layouts may then be used for monitoring purposes with conventional four-point configurations or specifically tailored measurement schedules following procedures like the ones described by Stummer et al. (2004) and Wilkinson et al. (2006).

Tomographic inversion performance

Synthetic example in analogy to the Ketzin storage site

At the Ketzin site near Berlin, Germany, more than 67 kt of CO_2 have been injected into a saline aquifer of the Upper Triassic at approximately 635 m depth until August 2013. Since the start of injection in June 2008, electrical resistivity tomography is part of a multi-method monitoring concept used to monitor the migration of CO_2 over time (Schmidt-Hattenberger et al., 2012; Bergmann et al., 2012). Geoelectrical measurements were realized by 15 stainless steel electrodes mounted on the electrically insulated borehole casing with a spacing of 10 m in the injection well and each of the two observation wells.

To validate the imaging quality of an optimized layout compared to equidistant installations, we consider a realistic two-dimensional CO_2 plume migration scenario between the injection and the first observation well. A three layer baseline model is interpreted from an induction log, performed under baseline conditions, as illustrated in Figure 10a. The dashed lines mark the averaged layer resistivities following the interpretations of Kiessling et al. (2010).
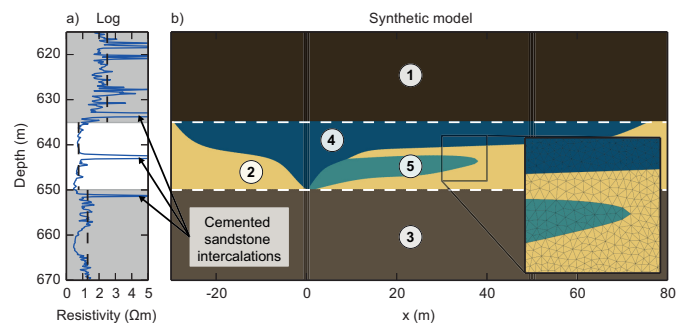
Figure 10: (a) Resistivity log of the injection well at Ketzin performed under baseline conditions. Dashed lines mark the interpreted layer resistivities following Kiessling et al. (2010). (b) Three-layer resistivity model used for forward modeling. The middle layer (2) is embedded with two segments representing areas of CO_2 migration (4 and 5) at two different timesteps. Resistivity values are assigned to the regions as listed in Tab. 1. The zoomed inlay illustrates the refined triangular discretization.

In addition to the baseline model (t_0), two consecutive timesteps t_1 and t_2 are considered. At time t_1, the CO_2 plume has passed the observation well at $x = 50$ m and is predominantly accommodated within the upper sandstone section of the reservoir horizon (marked with region number 4 in Figure 10b). Timestep t_2 represents a split of the CO_2 plume along the cemented sandstone intercalation (marked with region number 5 in Figure 10b), which is assumed to be impervious (Norden et al., 2010). This scenario is used to investigate the sensitivity to small-scale changes within the reservoir.

Forward modeling

To generate the synthetic data sets, resistivity values were assigned to the different region numbers in Fig. 10 as listed in Tab. 1. These values stem from experiments under in-situ conditions performed by Kummerow and Spangenberg (2011) assuming a brine/CO_2 mixture of equal parts for the regions occupied by CO_2 (region numbers 4 and 5 in Figure 10b).

Forward modeling was performed on a highly refined mesh with $\approx 250{,}000$ triangular cells allowing for a smooth and realistic plume shape as illustrated by the zoomed inlay in Figure 10b. The forward responses for all timesteps were calculated for the current Ketzin installation and the layout resulting from the optimization process. A conventional bipole-bipole set was used with inner bipole spacings of one and two unit electrode spacings for all possible separations between two bipoles. Prior to inversion, all data sets were contaminated with 3% uncorrelated noise and a voltage error of $5\,\mu V$ assuming an injection current of $1.0\,A$.

Tomographic inversion

For the inversion, measurements with an absolute geometric factor larger than $5 \cdot 10^5$ were removed resulting in slightly more than 1,500 data points. Regularization strength λ was varied iteratively to fit the data to the prescribed error level (i.e. $\lambda = 20$ led to convergence after 5-8 iterations). The median of the apparent resistivity values was used as a starting and reference model for the inversion of the baseline data set. From that point on, $\mathbf{m_{est}}(t_{n-1})$ served as the start and reference model for the inversion of $\mathbf{d_{obs}}(t_n)$. Figure 11 shows the underlying resistivity model (Figure 11a) and the corresponding inversion results obtained with the Ketzin layout and the optimized setup (Figure 11d, g). The true model and the inversion results at t_1 and t_2 are visualized as the ratio to the respective previous timestep.

To quantify the deviation from the true model shown in the upper row of Figure 11 (a-c), the Pearson correlation coefficient r is calculated for each tomographic reconstruction and plotted onto the respective images. While the baseline model is better imaged by the Ketzin layout due to the higher resolution in the caprock and baserock regions, the model at timestep t_1 is better resolved by the optimized layout, although the general CO_2 distribution can be properly resolved by means of both. At time t_2, the higher resolution of the optimized layout becomes apparent, as it is superior in reconstructing the subtle change in the lower half of the target horizon.

A comparison of the resolution properties of both layouts is shown in Figure 12. Figure 12a and Figure 12b show the resolution radii of the Ketzin layout and the optimized layout according to equation 6 with equal regularization strengths to allow for an objective comparison Maurer and Friedel (2006).

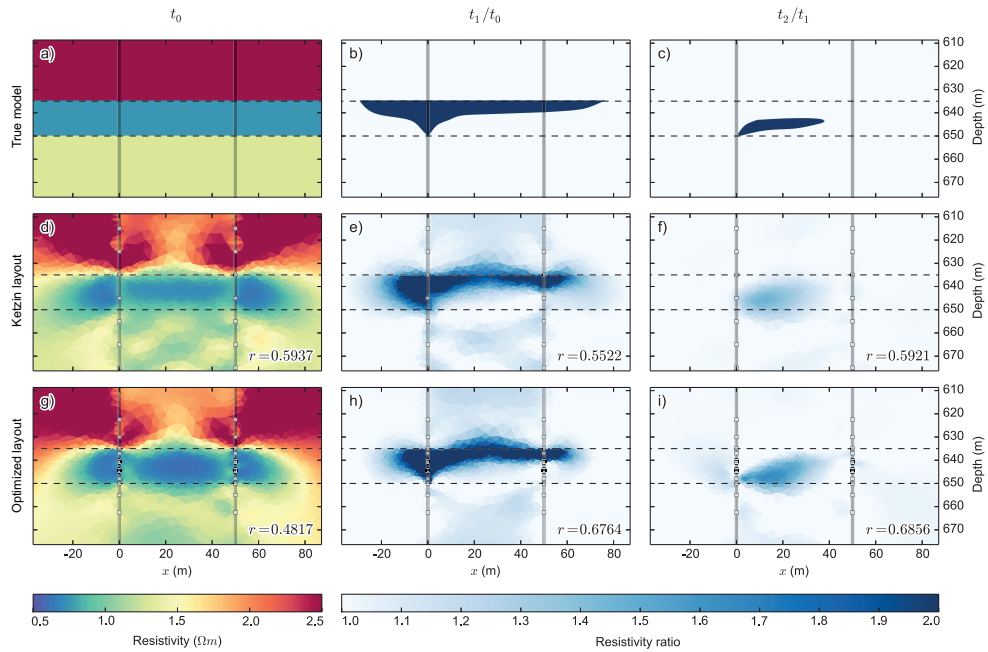Both layouts exhibit resolution radii ranging from a few
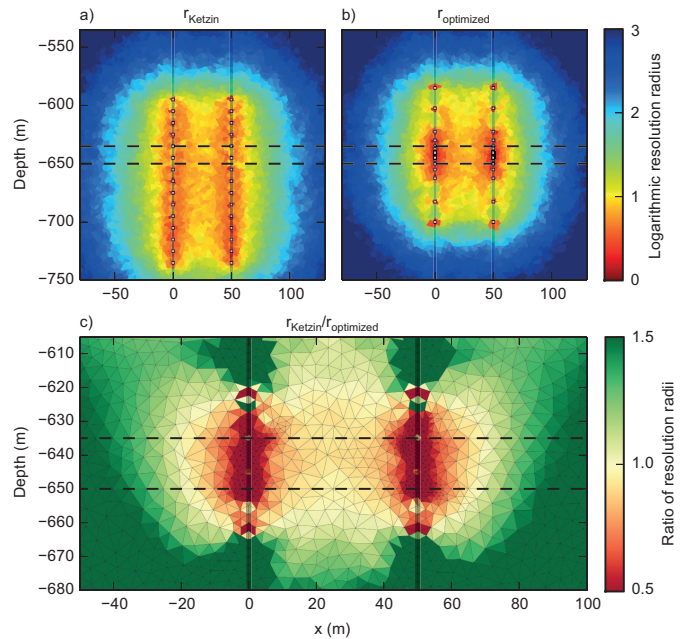
Figure 12: Logarithmic resolution radii of the Ketzin layout (a) and the optimized layout (b) and the corresponding ratio within the target horizon (c).

meters close to the electrodes approximately up to 10 m in the region between both boreholes. Further away from the boreholes, resolution decreases rapidly. An inspection of the corresponding ratio (Figure 12c) emphasizes that the optimized layout has its highest benefit close to the electrodes and in the region between both boreholes, whereas the Ketzin layout has smaller resolution radii further away from the boreholes and in the caprock and baserock regions, which were not in the focus of the optimization. This is in agreement with the superior tomographic reconstruction of the subtle change at t_2 (Figure 11i). Since the electrode spacing of 10 m of the Ketzin layout is comparably sparse with regard to the thickness of the target horizon (≈ 15 m), sensitivity to small-scale reservoir changes is challenged (Figure 11f). A refinement of the electrode spacing within the target horizon, as proposed by the optimization procedure presented, would have increased the imaging capability of the monitoring system with regard to small-scale reservoir changes over time.

Since resolution improvements outside of the target are neglected in the evaluation function (equation 7), the optimized array is focused on the target. We have chosen this very strict evaluation function to emphasize that even if resolution improvements outside of the target are neglected, electrodes outside of the target are important. Yet attention should be paid to limited resolution in the caprock and baserock regions in real monitoring applications when only resolution improvements in the reservoir are evaluated during the optimization process. The installation of additional electrodes at important indicator horizons is indispensable to verify storage integrity.

Table 1: Resistivity values at three individual timesteps assigned to the region numbers of the forward model (Figure 10). The resistivity values are based on laboratory experiments under in-situ conditions by Kummerow and Spangenberg (2011).

Timestep	Region number				
	1	2	3	4	5
t_0	2.5 Ωm	0.75 Ωm	1.3 Ωm	0.75 Ωm	0.75 Ωm
t_1	2.5 Ωm	0.75 Ωm	1.3 Ωm	2.0 Ωm	0.75 Ωm
t_2	2.5 Ωm	0.75 Ωm	1.3 Ωm	2.0 Ωm	2.0 Ωm

Figure 11: True resistivity model (a-c) and the corresponding inversion results obtained with the Ketzin (d-f) and the optimized layout (g-i) with an equal number of electrodes. The first column shows the absolute baseline model (t_0), whereas the second and the third column show the resistivity increases at times t_1 and t_2 in comparison to the respective previous timestep. Deviations from the true model are quantified by the Pearson correlation coefficient r for each tomographic reconstruction.

CONCLUSIONS

Reliable monitoring systems are a matter of utmost importance in the context of geological CO_2 storage and other applications. The resolution offered by geoelectrical installations within the monitoring target can be maximized by a refinement of the electrode spacing within the reservoir horizon, while a few electrodes in the caprock and baserock region are equally important to allow for an improvement of the model resolution by new linear independent measurement configurations. In the absence of pronounced borehole deviations and anisotropic heterogeneity, the electrode arrangements are symmetric for homogeneous and layered models. Conductive and resistive contrasts of the target horizon showed no significant change of the optimized layouts when its resistivity was altered up to a factor of four.

The sensitivities of all possible pole-pole measurements with a single electrode and the other electrodes in the survey layout have proven to be a valid means to characterize the goodness of a specific electrode location. Consideration of all conceivable non-reciprocal four-point configurations led to comparable electrode positions, while being computationally considerably more cumbersome. Inversion of synthetic data and a comparison of the resolution properties revealed improved imaging capabilities and higher sensitivity to subtle changes of the optimized layouts in comparison to the equidistant installation at Ketzin.

As a final remark, we would like to emphasize that a focused installation of permanent electrodes based on the method presented, or variants thereof, implicitly requires the target to be well characterized. In the absence of reliable a priori information, equidistant electrode layouts should be the first choice to circumvent the risk of defocussing. For symmetric crosshole scenarios with a known target layer and without significant resistivity contrasts, closely spaced target electrodes may suffice as a quick and practical measure to improve the spatial resolution in the horizon of interest. Nonetheless, detailed resolution analyses are always advisable prior to permanent installations. In this regard, the optimization approach presented can assist practitioners to increase the reliability and monetary efficiency of such permanent electrode installations particularly at, but not limited to, future underground storage sites.

Further advantage of optimized electrode layouts is expected for more complex and non-symmetric targets (e.g. dipping horizons, fault monitoring). Future site-specific research may apply the method in three dimensions and incorporate practical constraints such as data error estimates.

ACKNOWLEDGMENTS

REFERENCES

Aster, R. C., B. Borchers, and C. H. Thurber, 2012, Parameter estimation and inverse problems, 2nd ed.: Academic Press.

Bergmann, P., C. Schmidt-Hattenberger, D. Kiessling, C. Rücker, T. Labitzke, J. Henninges, G. Baumann, and H. Schütt, 2012, Surface-downhole electrical resistivity tomography applied to monitoring of CO_2 storage at Ketzin, Germany: Geophysics, **77**, B253–B267, DOI: 10.1190/geo2011-0515.1.

Bing, Z., and S. Greenhalgh, 2000, Cross-hole resistivity tomography using different electrode configurations: Geophysical Prospecting, **48**, 887–912, DOI: 10.1046/j.1365-2478.2000.00220.x.

Binley, A., and A. Kemna, 2005, DC resistivity and induced polarization methods, *in* Hydrogeophysics: Springer Netherlands, **50**, 129–156.

Blome, M., H. Maurer, and S. A. Greenhalgh, 2011, Geoelectric experimental design - Efficient acquisition and exploitation of complete pole-bipole data sets: Geophysics, **76**, F15–F26, DOI: 10.1190/1.3511350.

Boschi, L., 2003, Measures of resolution in global body wave tomography: Geophysical Research Letters, **30**, DOI: 10.1029/2003GL018222.

Breen, S. J., C. R. Carrigan, D. J. LaBrecque, and R. L. Detwiler, 2012, Bench-scale experiments to evaluate electrical resistivity tomography as a monitoring tool for geologic CO_2 sequestration: International Journal of Greenhouse Gas Control, **9**, 484–494, DOI: 10.1016/j.ijggc.2012.04.009.

Carrigan, C., X. Yang, D. J. LaBrecque, D. Larsen, D. Freeman, A. L. Ramirez, W. Daily, R. Aines, R. Newmark, J. Friedmann, and S. Hovorka, 2013, Electrical resistance tomographic monitoring of CO_2 movement in deep geologic reservoirs: International Journal of Greenhouse Gas Control, **18**, 401–408, DOI: 10.1016/j.ijggc.2013.04.016.

Christensen, N., D. Sherlock, and K. Dodds, 2006, Monitoring CO_2 injection with cross-hole electrical resistivity tomography: Exploration Geophysics, **37**, 44–49, DOI: 10.1071/EG06044.

Coscia, I., L. Marescot, H. Maurer, S. Greenhalgh, and N. Linde, 2008, Experimental design for crosshole electrical resistivity tomography data sets: Presented at the Near Surface 2008 - 14th European Meeting of Environmental and Engineering Geophysics, Krakow, Poland, 15 - 17 September, Extended Abstract B23.

Daily, W., A. Ramirez, D. LaBrecque, and J. Nitao, 1992, Electrical resistivity tomography of vadose water movement: Water Resources Research, **28**, 1429–1442, DOI: 10.1029/91WR03087.

Deceuster, J., O. Kaufmann, and M. Van Camp, 2013,

Automated identification of changes in electrode contact properties for long-term permanent ERT monitoring experiments: Geophysics, **78**, E79–E94, DOI: 10.1190/GEO2012-0088.1.

Friedel, S., 2003, Resolution, stability and efficiency of resistivity tomography estimated from a generalized inverse approach: Geophysical Journal International, **153**, 305–316, DOI: 10.1046/j.1365-246X.2003.01890.x.

Furman, A., T. P. A. Ferré, and G. L. Heath, 2007, Spatial focusing of geoelectrical resistivity surveys considering geologic and hydrologic layering: Geophysics, **72**, F65–F73, DOI: 10.1190/1.2433737.

Günther, T., C. Rücker, and K. Spitzer, 2006, Three-dimensional modelling and inversion of dc resistivity data incorporating topography - II. Inversion: Geophysical Journal International, **166**, 506–517, DOI: 10.1111/j.1365-246X.2006.03010.x.

Kemna, A., 2000, Tomographic inversion of complex resistivity: Theory and application: Der Andere Verlag. Berichte des Institutes für Geophysik der Ruhr-Universität Bochum: Reihe A.

Kiessling, D., C. Schmidt-Hattenberger, H. Schuett, F. R. Schilling, K. Krueger, B. Schoebel, E. Danckwardt, and J. Kummerow, 2010, Geoelectrical methods for monitoring geological CO_2 storage: First results from cross-hole and surface-downhole measurements from the CO2SINK test site at Ketzin (Germany): International Journal of Greenhouse Gas Control, **4**, 816–826, DOI: 10.1016/j.ijggc.2010.05.001.

Köhler, S., J. Zemke, W. Becker, J. Wiebach, A. Liebscher, F. Möller, and A. Bannach, 2013, Operational reservoir monitoring at the CO_2 pilot storage site Ketzin, Germany, *in* Clean Energy Systems in the Subsurface: Production, Storage and Conversion: Springer Berlin Heidelberg, Springer Series in Geomechanics and Geoengineering, 53–63.

Kummerow, J., and E. Spangenberg, 2011, Experimental evaluation of the impact of the interactions of CO_2-SO_2, brine, and reservoir rock on petrophysical properties: A case study from the Ketzin test site, Germany: Geochemistry, Geophysics, Geosystems, **12**, Q05010, DOI: 10.1029/2010GC003469.

Loke, M. H., P. B. Wilkinson, and J. E. Chambers, 2010, Fast computation of optimized electrode arrays for 2d resistivity surveys: Computers & Geosciences, **36**, 1414–1426, DOI: 10.1016/j.cageo.2010.03.016.

Loke, M. H., P. B. Wilkinson, J. E. Chambers, and M. Strutt, 2014, Optimized arrays for 2D cross-borehole electrical tomography surveys: Geophysical Prospecting, **62**, 172–189, DOI: 10.1111/1365-2478.12072.

Martens, S., T. Kempka, A. Liebscher, S. Lth, F. Möller, A. Myrttinen, B. Norden, C. Schmidt-Hattenberger, M. Zimmer, and M. Kühn, 2012, Europes longest-operating on-shore CO_2 storage site at Ketzin, Germany: a progress report after three years of injection: Environmental Earth Sciences, **67**, 323–334, DOI: 10.1007/s12665-012-1672-5.

Maurer, H., A. Curtis, and D. E. Boerner, 2010, Recent advances in optimized geophysical survey design: Geophysics, **75**, 75A177–75A194, DOI: 10.1190/1.3484194.

Maurer, H., and S. Friedel, 2006, Outer-space sensitivities in geoelectrical tomography: Geophysics, **71**, G93–G96, DOI: 10.1190/1.2194891.

Norden, B., A. Föster, D. Vu-Hoang, F. Marcelis, N. Springer, and I. Le Nir, 2010, Lithological and petrophysical core-log interpretation in CO2SINK, the European CO_2 onshore research storage and verification project: SPE Reservoir Evaluation & Engineering, **13**, 179–192, DOI: 10.2118/115247-PA.

Oldenborger, G. A., and P. S. Routh, 2009, The point-spread function measure of resolution for the 3-D electrical resistivity experiment: Geophysical Journal International, **176**, 405–414, DOI: 10.1111/j.1365-246X.2008.04003.x.

Perri, M. T., G. Cassiani, I. Gervasio, R. Deiana, and A. Binley, 2012, A saline tracer test monitored via both surface and cross-borehole electrical resistivity tomography: Comparison of time-lapse results: Journal of Applied Geophysics, **79**, 6–16, DOI: 10.1016/j.jappgeo.2011.12.011.

Ramirez, A. L., R. L. Newmark, and W. D. Daily, 2003, Monitoring carbon dioxide floods using electrical resistance tomography (ERT): Sensitivity studies: Journal of Environmental and Engineering Geophysics, **8**, 187–208, DOI: 10.4133/JEEG8.3.187.

Rücker, C., T. Günther, and K. Spitzer, 2006, Three-dimensional modelling and inversion of dc resistivity data incorporating topography - I. Modelling: Geophysical Journal International, **166**, 495–505, DOI: 10.1111/j.1365-246X.2006.03010.x.

Schmidt-Hattenberger, C., P. Bergmann, T. Labitzke, S. Schröder, K. Krüger, C. Rücker, and H. Schütt, 2012, A modular geoelectrical monitoring system as part of the surveillance concept in CO_2 storage projects: Energy Procedia, **23**, 400–407, DOI: 10.1016/j.egypro.2012.06.062.

Slater, L., A. Binley, W. Daily, and R. Johnson, 2000, Cross-hole electrical imaging of a controlled saline tracer injection: Journal of Applied Geophysics, **44**, 85–102, DOI: 10.1016/S0926-9851(00)00002-1.

Soldati, G., L. Boschi, and A. Piersanti, 2006, Global seismic tomography and modern parallel computers: Annals of Geophysics, **49**, DOI: 10.4401/ag-4407.

Stummer, P., H. Maurer, and A. G. Green, 2004, Experimental design: Electrical resistivity data sets that provide optimum subsurface information: Geophysics, **69**, 120–139, DOI: 10.1190/1.1649381.

Wang, Q., X. Zhang, Y. Zhang, and Q. Yi, 2013, AUGEM: Automatically generate high performance dense linear algebra kernels on x86 CPUs: Proceedings of the International Conference on High Performance Computing, Networking, Storage and Analysis, ACM, 25:1–25:12.

Wilkinson, P. B., M. H. Loke, P. I. Meldrum, J. E. Chambers, O. Kuras, D. A. Gunn, and R. Ogilvy, 2012,

Practical aspects of applied optimized survey design for electrical resistvity tomography: Geophysical Journal International, **189**, 428–440, DOI: 10.1111/j.1365-246X.2012.05372.x.

Wilkinson, P. B., P. I. Meldrum, J. E. Chambers, O. Kuras, and R. D. Ogilvy, 2006, Improved strategies for the automatic selection of optimized sets of electrical resistivity tomography measurement configurations: Geophysical Journal International, **167**, 1119–1126, DOI: 10.1111/j.1365-246X.2006.03196.x.

Wilkinson, P. B., P. I. Meldrum, O. Kuras, J. E. Chambers, S. J. Holyoake, and R. D. Ogilvy, 2010, High-resolution electrical resistivity tomography monitoring of a tracer test in a confined aquifer: Journal of Applied Geophysics, **70**, 268–276, DOI: 10.1016/j.jappgeo.2009.08.001.

Xu, B., and M. Noel, 1993, On the completeness of data sets with multielectrode systems for electrical resistivity surveys: Geophysical Prospecting, **41**, 791–801, DOI: 10.1111/j.1365-2478.1993.tb00885.x.